Analyzing powers and cross sections of $\vec{p}p \rightarrow pn\pi^+$ near threshold

R. W. Flammang, W. W. Daehnick, S. A. Dytman, D. J. Tedeschi,* R. A. Thompson, and T. Vrana
Department of Physics and Astronomy, University of Pittsburgh, Pittsburgh, Pennsylvania 15260

C. C. Foster, J. G. Hardie,† W. W. Jacobs, T. Rinckel, and E. J. Stephenson
Indiana University Cyclotron Facility, Bloomington, Indiana 47408

P. V. Pancella
Physics Department, Western Michigan University, Kalamazoo, Michigan 49007

W. K. Brooks
Thomas Jefferson National Accelerator Facility, Newport News, Virginia 23606
(Received 2 February 1998)

Analyzing powers for $\vec{p}p \rightarrow pn\pi^+$ were measured for the first time close to threshold at beam energies that yield maximum pion momentum fractions ($\eta \equiv p_{\text{c.m.}}^{\max}/m_\pi c$) of $\eta = 0.22$, 0.42, and 0.50, and enable a decomposition of the low order partial waves. Cross sections were measured at seven different beam energies with $\eta = 0.07$, 0.17, 0.22, 0.28, 0.34, 0.42, and 0.50. The analysis shows that pion s-wave channels dominate the reaction. The p-wave channel containing the Δ resonance contributes, at $\eta = 0.22$, less than one-tenth of the total cross section and less than one-third of the total cross section at $\eta = 0.42$ and 0.50. The nonresonant p-wave channel contributes less than 1% of the cross section at these three energies. [S0556-2813(98)07406-8]

PACS number(s): 25.10.+s, 11.40.Ha, 13.75.Cs, 21.30.Cb

I. INTRODUCTION

Pion exchange is a crucial mechanism for all strong interactions between nucleons at low and intermediate energies. At low energies with small momentum transfers, the πNN vertex and s-wave rescattering contribute the most important graphs in the $NN \rightarrow NN$ interaction [1].

This work describes the measurement of differential cross sections, analyzing powers, and the partial-wave amplitudes deduced from them in the region near the pion-production threshold. Close to threshold, the contribution from the Δ and pion p waves is expected to disappear. Thus, the πNN vertex, s-wave rescattering, and perhaps heavy-meson exchanges are primarily active in near-threshold $NN \rightarrow NN\pi$ reactions. Behavior at the vertex for large momentum transfers, where exchanged bosons heavier than the pion can become important, are best tested by studying pion production in NN collisions close to threshold.

The form factor of the πNN vertex has been described with cutoff parameters varying with the kind of reaction described. With one exception [2], the cutoff values deduced from on-shell pion reactions have tended to be less than 800 MeV [3–6], while those deduced from NN elastic scattering tend to be larger than 1.1 GeV [7,8]. At present this discrepancy is not resolved, although more sophisticated treatments may eliminate the need for different form factors for different reactions [9].

Early theoretical work on near-threshold pion production used phase space considerations and isospin conservation to deduce the energy dependence of the cross section for $NN \rightarrow NN\pi$ reactions [10,11]. Woodruff [12] and Koltun and Reitan [13] used empirical knowledge of the NN potential and the assumption of s-wave dominance to calculate total cross sections. Later, the use of partially conserved axial-vector current (PCAC) and soft pion theorems facilitated a calculation of cross sections near threshold [14].

Since 1990, with the advent of new technology developed at IUCF and other facilities around the world, the study of near-threshold $NN \rightarrow NN\pi$ has attracted increasing attention. Total cross sections for $pp \rightarrow pp\pi^0$ have been measured [15–17]. Cross sections [18] and analyzing powers [19,20] for $\vec{p}p \rightarrow d\pi^+$ have also been measured near threshold. Before 1990 the lowest energy measurements of $pp \rightarrow pn\pi^+$ were those of Falk *et al.* [21] which were over 100 MeV above threshold. Today, the measurements of our collaboration [22,23] have extended our knowledge of this reaction down to less than 1 MeV above threshold. The present work and its associated Letter [24] mark the first time analyzing powers for $\vec{p}p \rightarrow pn\pi^+$ near threshold have been measured.

The new cross sections for $pp \rightarrow pp\pi^0$ have inspired numerous calculations for that reaction. Nonetheless, a consensus on the proper approach to this problem has not been reached. The approach previously used by Koltun and Reitan [13] underpredicted the observed cross sections by a factor of 5 [25]. Two competing mechanisms have been proposed to make up for this shortfall: the exchange of heavy mesons (σ,ρ,ω) via ''z graphs'' [see Fig. 1(c)] [26–28] and the off-shell extrapolation of the vertex form factor [2]. Researchers disagree whether either or both mechanisms can account for

*Present address: Department of Physics and Astronomy, University of South Carolina, Columbia, SC 29208.

†Present address: Department of Physics and Computer Science, Christopher Newport University, Newport News, VA 23606.

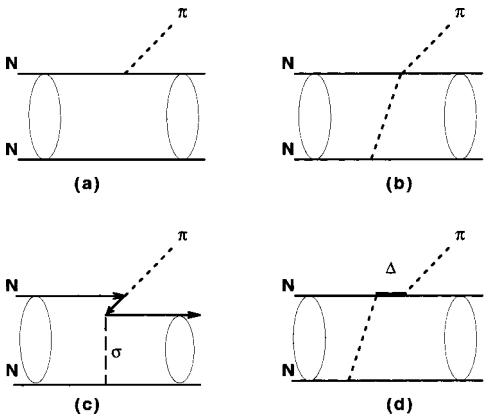

FIG. 1. Feynman graphs for the reaction $pp \rightarrow pn\pi^+$, showing the direct production term (a), the pion rescattering term (b), and a heavy-meson-exchange term (c), as well as the contribution of the Δ (d).

the discrepancy without including the Δ channel or some other effect [29–34].

Although there have been many publications on the reaction $pp \rightarrow pp\pi^0$ as well as on $NN \rightarrow d\pi$ [31,33], until recently, little work on $pp \rightarrow pn\pi^+$ has been published. When the present experiment first ran in 1995, the paper of Schillaci, Silbar, and Young [14] and an unpublished work by Lee [6] were the only theoretical studies of this reaction. Today, Fäldt and Wilkin have extrapolated $pp \rightarrow d\pi^+$ to the unbound pn case [35,36]. A new relativistic calculation by Engel *et al.* [37], which includes all meson exchanges as well as the Δ channel, agrees well with cross sections for $pp \rightarrow pn\pi^+$ and $pp \rightarrow pp\pi^0$ over a wide range of energies, but underpredicts by a factor of 2–4 near threshold. Recent refinements which take into account the final-state interactions [38] have made this work applicable in the threshold region. Unlike the previous predictions for $pp \rightarrow pp\pi^0$, these models [35–38] do not assume that the reactions are purely s wave, and so they should be able to predict analyzing powers. Reference [36] and the recent thesis of Hanhart [39] give the first published calculations of analyzing powers for this reaction.

In contrast to the calculations for $pp\pi^0$ final states, recent work [6,38] on the $pn\pi^+$ reaction suggests that it may be dominated by the πNN rescattering term. If this is true, the $pn\pi^+$ cross sections should allow the extraction of the direct-production and rescattering strengths of the πNN interaction.

To shed light on these issues, kinematically complete measurements of the differential cross sections were previously published for $pp \rightarrow pn\pi^+$ near threshold by the present collaboration in [22]. Some simplifying assumptions together with the cross sections allowed preliminary insights into the partial-wave composition of the reaction. The analysis of the unpolarized $pp \rightarrow pn\pi^+$ differential cross sections at 294, 300, and 320 MeV had provided evidence that the contribution of pion p waves was negligible at 294 MeV but became significant at 320 MeV. This provides strong evidence that these data are sensitive to the nonresonant πNN vertex. The present experiment has confirmed and extended the cross section measurements of Ref. [23] and also measured the analyzing powers. With the new data, a partial-wave analysis of the reaction can now be done. In the present work, such an analysis is now available for unbound $NN\pi$ close to threshold where only a few terms contribute. These new results are discussed below.

II. EXPERIMENTAL APPARATUS

This experiment, CE-38 at IUCF, is an extension of previous experiments [22,23], which measured the differential and total cross sections of $pp \rightarrow pn\pi^+$. The apparatus used here has been described in detail previously [23]. The large acceptance detectors measured the four-momenta of the ejected p and n, allowing the reconstruction of the pion four-momentum. Measurement of the p and n four-momenta allows for a kinematically complete reconstruction of the pion cross sections and analyzing powers.

The Cooler Ring of IUCF provided a recirculating polarized proton beam, which was cooled to an energy spread of $\Delta E/E \sim 10^{-4}$, of low emittance and high intensity ($\sim 100\ \mu$A). It intersected a thin ($\sim 3 \times 10^{15}$ atoms/cm^2) gas jet of pure hydrogen. The reaction nucleons were ejected in a narrow cone in the forward direction. The nucleons traveled about 1 m through vacuum before entering the air to travel to the detector stacks (see Fig. 2). A wide-gap 6° dipole magnet swept the reaction protons leftward towards a proton detector arm consisting of drift chambers, a fast timing ΔE scintillator, E detectors, and veto scintillators. The magnet acted as a low resolution spectrometer, allowing for discrimination between true events and quasielastic back-

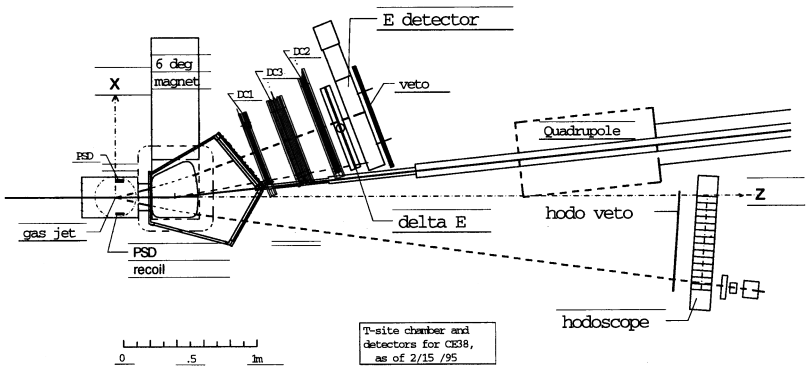

FIG. 2. Scale drawing of the apparatus of CE-38. Beam approaches from the left. Top view of the target, 6° ring magnet, and detectors.

TABLE I. Kinematic parameters dependent on beam energy, showing the maximum pion momentum fraction η, the minimum nucleon energy in the laboratory frame, $E_{\min}$, the maximum nucleon energy in the laboratory, $E_{\max}$, and the maximum nucleon angle in the laboratory frame, $\theta_{\max}$. All energies are in MeV.

E_{beam}	η	$E_{\min}$	$E_{\max}$	$\theta_{\max}$
293.0	0.07	63.5	78.3	2.9°
297.0	0.17	54.1	91.4	7.2°
300.0	0.22	50.3	98.3	9.2°
305.0	0.28	45.7	107.8	11.8°
310.0	0.34	42.3	116.2	13.8°
320.0	0.42	37.3	131.3	17.1°
330.0	0.50	33.6	144.9	19.7°

ground. The neutrons, unbent by the magnet, exit through a 3-mm-thick aluminum window and continue straight to a hodoscope. The neutron energy was measured by making a time-of-flight comparison with the detected protons.

Table I shows the kinematic ranges of the reaction nucleons in the laboratory. Because of the large negative Q value for pion production, the reaction cone of the two detected nucleons was quite narrow, allowing for good acceptance close to threshold. As the cone opens up, we begin to lose events, as is shown in Fig. 3. The geometrical effects of the neutron and proton detectors and the magnet pole faces are accounted for, but the effects of the detector efficiencies are not included in this particular figure.

A. Beam and target

The energy of the beam was determined by the frequency of the synchrotron rf in the storage ring and the circumference of the beam orbit inside the ring by the relation

$$v = \frac{Cf}{n}, \tag{1}$$

where v is the speed of the beam protons, C is the ring circumference, f is the synchrotron frequency, and n is the

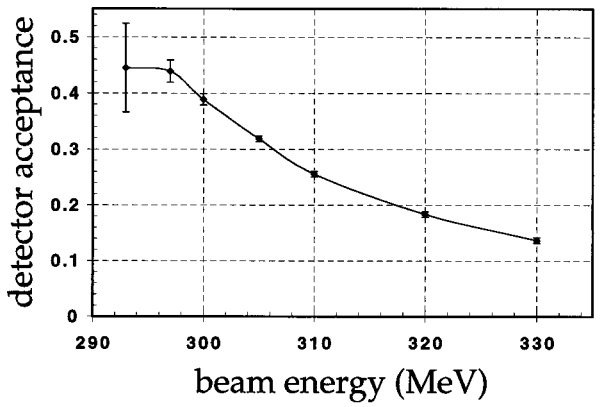

FIG. 3. Monte Carlo calculation of the geometrical n-p acceptance for coincidences as a function of beam energy. The uncertainties at 293 and 297 MeV are due to the 0.2° uncertainty of the beam direction, which has a greater effect at low energies where the reaction cone is very narrow.

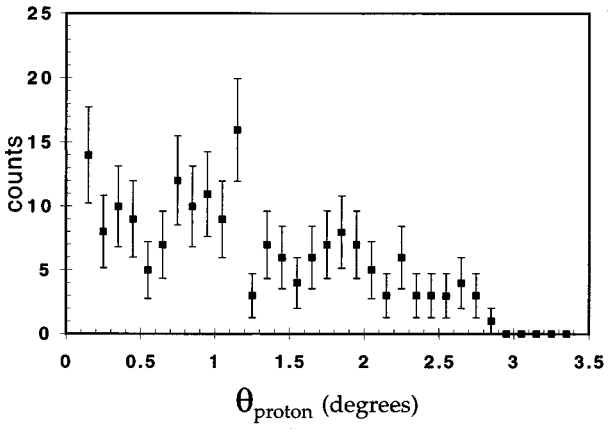

FIG. 4. Opening angle of reaction protons at 293 MeV. Given a beam circulation frequency of 2.2376 MHz, the opening angle for protons should be 2.7° for $C=8675$ cm, 2.9° for $C=8676$ cm, and 3.1° for $C=8677$ cm.

harmonic of the ring (a whole number). The frequency is known to six significant figures, and so knowledge of the beam energy is limited by the uncertainty of the orbit circumference. The best value for the beam circumference was obtained by determining the 293 MeV beam energy from observations of the maximum angle of the reaction-proton cone (see Fig. 4). Our best measurement of this angle determined the outer edge to be $2.9\pm0.2°$, yielding $C=8676\pm1$ cm and an uncertainty in the mean beam energy of ±110 keV. This agrees well with the circumference ($=8677\pm1$ cm) used by the local experimenters and operators at IUCF [40] in 1995, when the present data were taken.

The direction of the incident beam was determined by surveys of the physical apparatus. To further verify the direction, a lead ''scraper'' target was installed for one run and p-Pb elastic scattering angular distributions were measured. The result was compared to well-known previously measured differential cross sections for p-Pb elastic scattering, which has very sharp minima at well-defined angles. By matching our measurements with the previous results [41], we verified our beam direction to within the 0.2° range permitted by varying tunes of the beam.

The target jet consisted of H_2 molecular gas cooled to 40 K. For the purposes of this experiment, the initial target kinetic energy was zero. The target density distribution peaked at $z=0$ with a full width at half maximum (FWHM) of about 1.1 cm. Low density tails extended out to $z=\pm7.5$ cm. The measurement of the density distribution and its extrapolation into the tail region followed the method described in our previous paper [23].

B. Proton detector arm

The proton detector stack contained three drift chambers with a position resolution of 0.3 mm, the first of which was positioned 1.1 m downstream of the target. Two of the drift chambers, labeled DC1 and DC2 in Fig. 2, contained x and y wire planes. A third chamber, DC3, in addition contained the so-called w plane, with wires running 45° to the x and y directions, which allowed it to distinguish trajectories in

events with overlapping charged particles.[1] The addition of DC3 to the detector stack provided desirable redundancy and ensured that the proton trajectories in 99.9% of our triggered events could be reconstructed.

The operation of the drift chambers is described in Ref. [23] except for three improvements mentioned here: The chambers contained a 50%-50% argon-ethane gas mixture which was bubbled through alcohol which was refrigerated to 1 °C, the voltage between the anode and cathode wires was kept near 2500 V, and DC3 was added to the stack (mentioned above). The introduction of alcohol to the gas mixture made a substantial improvement to the longevity of the chambers by reducing the buildup of carbon on the wires. This allowed the chambers to run at higher voltages where they generated stronger signals, which are less susceptible to noise and electrical oscillations in the LeCroy 2735DC amplifier cards used in the chambers.

Mounted behind the drift chambers was a large, 35×65-cm-wide, and 0.3-cm-thick plastic ΔE detector viewed through adiabatic light pipes by two fast phototubes (Amperex 2220 PMT) on either end. The ΔE signal served as a timing base line for the neutron time-of-flight calculations and also yielded an energy signal which was used to generate a particle identification (PID) spectrum. Studies using an ultraviolet laser inducing light production in several of our scintillation detectors simultaneously measured the time resolution of the ΔE to be 0.28 ns [42].

After punching through the ΔE detector, the reaction protons stopped in one of the five $7.5\times12.7\times60$-cm plastic scintillator ''E'' bars stacked at the rear of the proton arm. The measured pulse heights were corrected for light attenuation in the bar [43], for light quenching in the organic scintillators, and for the energy loss in the 0.6 g/cm^2 of material in front of the E bars. Details of the energy calibration can be found in Ref. [42].

Behind the E bars were two thin scintillator paddles that served as veto detectors. They flagged particles that did not stop in the E bars and were used to reject events.

C. Neutron hodoscope

The neutron hodoscope has been described previously [44]. It comprised fourteen 120-cm-tall, plastic, vertical scintillator bars with Amperex XP2252H phototubes at each end and was positioned at beam right 4.5 m downstream of the target. Each bar was 15 cm thick and detected about 13% of the reaction neutrons incident upon it. The x position was determined by the location of the 5-cm-wide bar which a neutron triggered. The y position was determined by the relative time difference between the signals received at the top and bottom phototubes; the y resolution, dependent on the energy deposited in the bar, ranged from 2.5 to 5 cm FWHM. In front of the hodoscope, an array of four thin veto paddles ensured that the particles triggering the hodoscope were neutral.

The neutron energies were determined by their time of flight, derived from the relative timing of the hodoscope and the proton fast-timing trigger. Time-of-flight energy determinations depend on the path length which, in our case, was uncertain within the thickness of the hodoscope, or 15 cm. This uncertainty determined the energy resolution of the detector, which was $\pm3.4\%$.

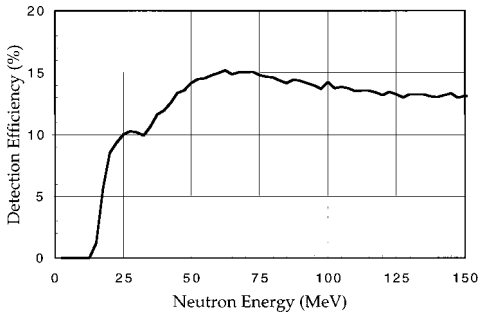

FIG. 5. The hodoscope neutron-detection efficiency as a function of the energy of the incident neutron. Monte Carlo calculation for a hodoscope bar with a pulse-height threshold equal to the light output of an 8.5 MeV electron. Similar curves were calculated for each of the 14 hodoscope bars, and a lookup table was used to generate event-by-event corrections.

The hodoscope's efficiency was determined using a Monte Carlo calculation written at Kent State University [45]. When given the scintillating material, detector geometry, neutron energy, and light detection thresholds as input, the code returns a detection efficiency as output. The efficiency depends on the neutron energy, and so the correction to the neutron counts was made by weighting each event by the inverse of the efficiency for its energy. A plot of the efficiency as a function of incident neutron energy for the hodoscope is shown in Fig. 5.

D. Luminosity monitor and polarization

In addition to the two detector arms mentioned above, there were two 7×45-mm position-sensitive silicon detectors (PSD's) 12 cm away from the target on both sides of the beam. The left PSD detected elastically scattered protons in coincidence with the hodoscope; the right PSD detected elastic events in coincidence with the proton arm detector stack. Event triggers which flagged these *elastic* coincidences in our event stream required the veto detectors in coincidence with the other detectors (i.e., the so-called ''veto'' detectors were used in the coincidence mode instead of the normal rejection mode).

The event stream monitored these pp elastic coincidences simultaneously with the measurement of pn coincidences. Since the cross section and analyzing power of pp elastic scattering are well known [46], these events were used for monitoring beam-target luminosity and beam polarization.

E. Event triggers

Events used in this analysis were of three different types and required the following hardware triggers to be recorded into the data stream.

(i) Pion candidates. These events required simultaneous counts in one of the hodoscope bars (both phototubes), the ΔE, and one of the E scintillators. They were vetoed by a

[1]Such as the p-p pair from $pp\pi^0$ final states or the $p\pi^+$ pair from $pn\pi^+$ final states.

TABLE II. Resolutions of the nucleon detectors. Only three of the quantities shown have a Gaussian distribution. The resolutions shown for the hodoscope x position and T_n are maximum errors determined by geometry.

Hodoscope x position	± 2.5 cm
Hodoscope y position	4.0 cm, FWHM
Hodoscope energy T_n	$\pm 3.4\%$
Drift chamber positions	0.30 mm, FWHM
E-detector energy	$\sim 2.5\%$, FWHM

count in any of the veto paddles in front of the hodoscope or behind the E bars.

(ii) Hodoscope-arm elastic protons. These events required counts in one of the hodoscope bars, in one of the hodoscope veto paddles, and in the left PSD.

(iii) Proton-arm elastic protons. These events required counts in the ΔE detector, one of the E scintillators, and in the right PSD. They were vetoed by counts in the hodoscope to prevent ambiguities with the pion-candidate trigger.

III. ANALYSIS

This experiment is a kinematically complete measurement of the pion differential cross section and analyzing power for the reaction $\vec{p}p \rightarrow pn\pi^+$. We measure the pion kinematic observables indirectly, by reconstructing them from the observed proton and neutron four-momenta,

$$P^{\mu}_{\pi} = P^{\mu}_{\text{beam}} + P^{\mu}_{\text{target}} - P^{\mu}_{p} - P^{\mu}_{n}. \tag{2}$$

The beam four-momentum is known from the beam energy and our definition of the z axis as being the beam direction. Because of mass differences between the two-nucleon systems of pp, pn, and d, comparisons between the reactions $pp \rightarrow pn\pi^+$, $pp \rightarrow d\pi^+$, and $pp \rightarrow pp\pi^0$ usually parametrize the energy in terms of η, the maximum pion momentum in the center-of-mass system in units of the pion mass.

In our E scintillators, we measure the reaction proton's kinetic energy T_p. The individual components of the three-momentum p_p are found by tracing the proton's trajectory through our seven drift-chamber planes, $1x$, $1y$, $2x$, $2y$, $3x$, $3y$, and $3w$. We perform a least squares fit to the chamber coordinates to determine the proton trajectory. To determine the initial momentum, we track the proton back to the $z=0$, or target, plane through the magnetic field. We take magnetic bending into account using the CERNLIB library subroutine NYRAP and a user-supplied function MAGF which we wrote based on the measured magnetic field map.

The energy of the neutron is determined by its time of flight, which is measured in relation to the proton. The momentum components are determined from the position measured by the hodoscope.

Resolutions. The finite detector resolutions in our hodoscope, E bars, and drift chambers introduce errors into our reconstruction of the pion four-momentum; a summary of these resolutions is shown in Table II. In addition to the random error listed for the E detectors, there is an additional systematic energy error due to the uncertainty of the fit of the energy calibration formula to the calibration points. The error in that fit is about 0.5 MeV in the 65–75 MeV range. Outside of that central range, the error grows as large as 2 MeV for 30-MeV protons, and 3 MeV for 120-MeV protons. The hodoscope's spatial resolution given in Table II is for the smallest pulse heights (equivalent to the light from 8.5 MeV electrons); neutrons that generate double this amount of light have resolutions as small as 2.5 cm FWHM [44].

TABLE III. Distribution of errors in the pion angular distribution deduced by a Monte Carlo simulation, shown as a function of cos θ in the center of mass.

Energy	η	Resolution of cos θ, FWHM
293 MeV	0.07	0.69
297 MeV	0.17	0.28
300 MeV	0.22	0.22
305 MeV	0.28	0.17
310 MeV	0.34	0.12
320 MeV	0.42	0.12
330 MeV	0.50	0.13

To understand the effects of these resolution functions on our pion angular distribution, we use a Monte Carlo model calculation, and compare the reconstructed angles with those that are calculated initially. The resulting pion cos θ resolution in the center of mass is shown in Table III for our seven beam energies. The FWHM for the pions is given; these resolutions are not Gaussian in shape, but are roughly triangular near the peak. In general, the resolution is worse for low energy pions whose reconstructed trajectories have large uncertainties due to errors in the determination of the p and n energies. At higher energies, these errors become smaller relative to the increasing pion energy.

A. Background elimination

Even at the largest angles seen by our proton detector ($\sim 18°$), the elastic $pp \rightarrow pp$ reaction at $T_{\text{beam}} = 320$ MeV has a cross section on the order of 20 mb/sr, which is 10 000 times larger than the $pp \rightarrow pn\pi^+$ cross section. Even if our veto paddles were 99.99% efficient, they would still let as many pn quasielastic elastic events slip through the trigger requirements as we have $pn\pi^+$ reaction events. In addition to the elastic pp events, we also see quasielastic protons and neutrons from the steel exit pipe of the magnet chamber where the beam halo is scraped off. There are so many of these background events that a significant number of them make accidental coincidences with counts in the hodoscope. A significant fraction (50–90 %) of our raw coincident triggers is spurious. This problem is most severe close to threshold.

Fast nucleons from quasielastic (p,pn) reactions dominate our background, but other kinds of spurious triggers are possible. At energies close to threshold, the strength of the channel $pp \rightarrow pp\pi^0$ rivals that of $pp \rightarrow pn\pi^+$. The neutral π^0 decays within $\sim 10^{-16}$ s into high energy photons which can occasionally trigger our hodoscope. One or more of the reaction protons could simultaneously trigger our proton arm.

We were able to eliminate these sources of background by the application of the following tests.

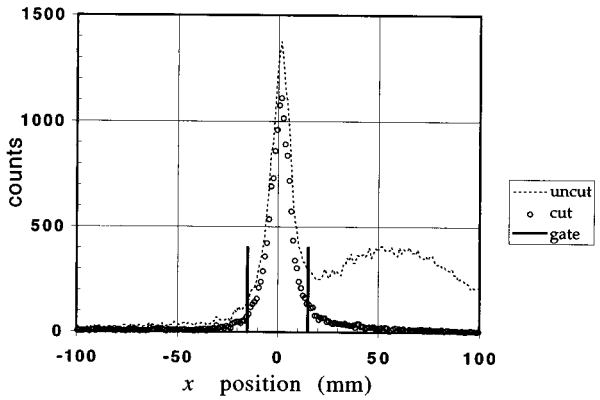

FIG. 6. Position in x of the intersection of the proton's trajectory with the $z=0$ plane. The uncut counts are shown as well as counts cut on the missing mass, PID, and y-vertex peaks. The x-vertex gate is shown in bold tick marks.

Kinematic limits. The kinematics of the reaction $pp \rightarrow pn\pi^+$ imposes strict limits on the allowed range of proton and neutron energies. We reject all events where we measure an energy that falls more than 5 MeV outside of these limits. This test eliminates spurious events associated with low energy background in the proton arm. It also excludes $pp \rightarrow pp\pi^0$ events which trigger the hodoscope; the photons from these events have a very short time of flight and cause our apparent neutron energy to be too high.

The vertex cut. The 6° bending magnet lets us make a spectrometer cut by eliminating all particles that do not trace back to the target. The x-y vertex cut alone eliminates most spurious counts from the data set. More than 90% of all counts that pass the vertex cut also pass both the missing mass and particle identification cuts.

Figure 6 shows the x vertex spectrum of this experiment. The cut we used is $-15\ \text{mm} < x < +15\ \text{mm}$. The vertex peak did not change shape from one beam energy to another. The spectrometer ensures that only protons which originated from the target and whose energy was measured correctly trace back to the $x=0$ point. The width of the peak is primarily the result of multiple scattering, along with detector resolutions and the gas-jet target's extension in z.

A similar cut was made on the y vertex. Although the y vertex does not contain spectrometric information, it still serves to eliminate counts which do not originate from the target.

Particle identification. The $E \times \Delta E$ particle identification (PID) cut eliminates most of the high energy protons which fail to trigger our veto paddles. This product is roughly constant for all T_p for the reaction events, but goes as $1/T_p^2$ for the protons that punch through, allowing many to be identified and eliminated.

The PID cut alone would not be sufficient for eliminating background. As many as 50% of all counts that pass this test do not originate from the target, and so it must be used in conjunction with a vertex cut.

Figure 7 shows the spectrum of the particle ID and its cut. The cut we used is 132 channels wide, centered about the reaction peak. The width of this PID peak does not change from bombarding energy to bombarding energy.

The missing mass cut. We calculate the missing pion mass from the nucleon kinematic variables by the relation

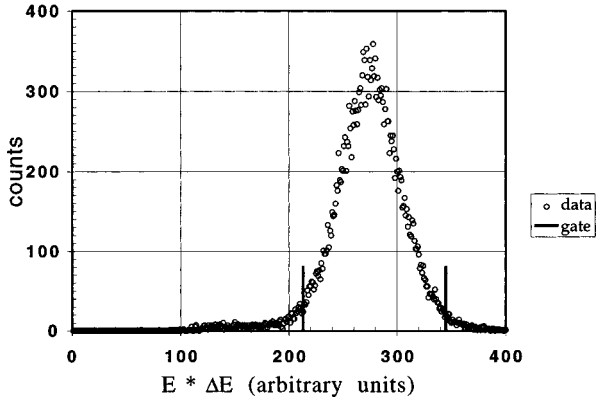

FIG. 7. Particle identification histogram $E \times \Delta E$, cut on the trace-back vertex. The PID gate is shown in bold tick marks.

$$m_\pi^2 = (P_\pi^\mu)^2 = (P_{\text{beam}}^\mu + P_{\text{target}}^\mu - P_p^\mu - P_n^\mu)^2. \qquad (3)$$

For a given incident energy, it is a function of the energies and scattering angles of the nucleons, and also of the opening angle between them. Because of this, testing whether the calculated missing mass is equal to the pion mass will eliminate spurious counts in the hodoscope as well as the proton arm.

Like the PID cut, the missing mass peak alone cannot generate a clean set of events. At 300 MeV, 33% of all events passing this cut do not originate from the target. At 320 and 330 MeV, 43% of the counts are spurious. This cut must be used in conjunction with a vertex cut.

The missing mass peak broadens with beam energy. Figures 8 and 9 show this peak for the 300- and 330-MeV runs. We cut out all events falling lower than 120 MeV.

Counting losses due to cuts. In addition to eliminating the spurious background, the above cuts also eliminate some of the reaction counts in our event stream. Nuclear reactions between reaction protons and carbon nuclei inside the E bars can cause erroneously low energy measurements that fall outside of the PID cut. The limited resolution of stopping protons can cause a small fraction of our good events to fall outside of the limits imposed by the cuts.

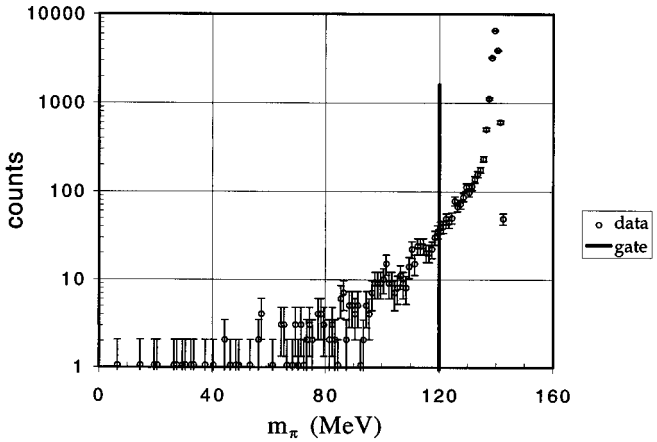

FIG. 8. Missing mass at 300 MeV, cut on the trace-back vertex. The missing mass gate cutoff is shown as a bold tick mark. $m_\pi = 139.6$ MeV.

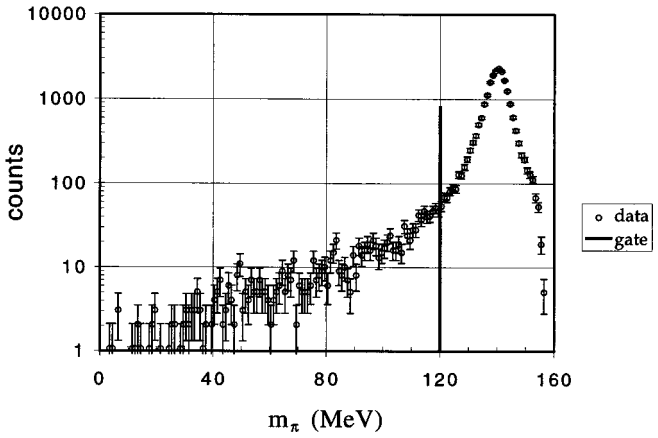

FIG. 9. Missing mass at 330 MeV, cut on the trace-back vertex. $m_\pi = 139.6$ MeV.

We estimate the number of these events by fitting a Gaussian shape to the tails of our PID and vertex distributions, and by calculating the fraction of the events missed. Correcting for the missing mass distribution is less straightforward. There, we see a peak followed by an extended tail. We modeled the losses with a Monte Carlo simulation which calculates a 6% loss, but does not predict the extended tail. If the extended tail is not background, we need an additional $\sim 7\%$ correction for a total of 13%. This ambiguity in the missing mass cut correction dominates the 8% uncertainty in the cross section due to cuts. Because the shape of the missing mass spectrum changes with beam energy, it is possible that this 8% error is systematic.

We estimate the total loss due to all of our software cuts to be about 17%, although one could estimate a loss as high as 22% by using the alternative missing mass distribution.

Figures 7–9 show where these cuts are applied. The PID and vertex spectra shown are for 320 MeV; the missing mass spectra are for 300- and 330-MeV beams. The kinematic energy limits and the vertex cut are applied to these curves.

WC redundancy. High count rates and background in drift chambers can cause multiple hits. If we determine the position from the wrong hit, we will calculate an erroneous value of p_p, which fails the tests. In about 25% of our events, at least one drift-chamber plane suffers one of these multiple triggers. We solve this problem by ignoring a drift-chamber plane with multiple triggers. Because we have seven drift-chamber planes (only four of which are needed to reconstruct an event), we can spare any single one of them (as well as some combinations of two or three of them) during an event in which they misfire. We make a χ^2 fit to the remaining unique position co-ordinates. This chamber requirement still leaves us with an overall drift-chamber efficiency of over 99%.

Beam halo and the target nozzle. In principle, background pions can be produced by protons in the beam halo reacting with the nuclei in the copper gas-jet target nozzle. Such background pions could not be completely eliminated by missing mass and particle ID cuts alone. To determine whether such background may be contaminating our analyzing powers, we placed successively restrictive cuts on the x and y vertices and the missing mass spectrum. We saw no systematic changes in our analyzing power and no changes at all outside of 1.2 times the statistical errors. We conclude that any background contamination which may be present does not alter our measurement outside of the listed errors.

B. Three-body acceptance

Our apparatus samples pions of all possible c.m. angles θ and ϕ at all seven of our beam energies. This remarkable feature is a result of our indirect detection of the pion. The two nucleons are limited by the detectors in the range of angles that can be seen, but the momenta of the third body are determined by reconstruction, not by a physical detector which is limited in solid angle. This freedom in three-body phase space makes the calculation of our acceptance too difficult to be done analytically, and so we simulate the experimental acceptance and resolution with a Monte Carlo calculation.

The geometrical arrangement of the detectors and the Monte Carlo simulation used are essentially the same as in Ref. [23]. The current version, however, estimates the effects of neutrons passing through the edges of the iron pole faces of the 6° bending magnet, which restricts the neutron acceptance. The uncertainty of this estimate is a large contributor to the uncertainty in the measurement of the angular distribution parameter C_2, discussed below. The Monte Carlo model assumes that any neutrons undergoing reactions with the iron are eliminated by the missing mass cut. The new code also takes into account the small changes in the detector placement and the addition of the third drift chamber. In the present experiment, the hodoscope was not moved during the course of data taking.

The Monte Carlo simulation uses the CERNLIB subroutine GENBOD to randomly calculate a three-body event with the masses of the pion, proton, and neutron for a given total energy in the center of mass. As discussed in Ref. [23], the code in GENBOD assigns a weight w_p to the event which makes it uniform in phase space. We multiply this phase-space weight by a second weight determined by the final-state NN interaction between the proton and neutron; the resulting event weight $w_e = w_p \times w$ is used in the histograms of the events.

The four-momenta of the two nucleons are then boosted into the laboratory frame and tracked forward toward our detector positions. The computed detector positions and nucleon energies of the accepted events are then smeared by the detector resolutions. The smeared coordinates are passed to our analysis software, which reconstructs the pion kinematics. The resulting pion observables are histogrammed (with weight w_e) to show the accepted pion spectrum.

The ratio of our initial and accepted $(dN/d\Omega)(\theta)$ histograms is our acceptance $a(\theta)$. We fit this function to a fifth order polynomial in order to smooth out statistical fluctuations from the Monte Carlo simulation. At the lowest energies, the distribution reconstructed from the measured np is sensitive to simulated errors in our energy calibration, which affect the linear term in our polynomial, $c_1 \cos\theta$, by 20% per MeV. It is less sensitive to errors in our angular calibration, which affect the quadratic term $c_2 \cos^2\theta$ by 2% per degree.

Uncertainties in the beam direction on the order of 0.2° result in systematic acceptance errors in the cross section of

15% at 293 MeV and 4% at 297 MeV. At 300 MeV and higher, these errors reduce to less than 1%.

The final-state interaction. The angular acceptance $a(\theta)$, as determined by the Monte Carlo simulation, is affected by the assumed form of the final-state interaction between the proton and neutron. The strongly attractive s-wave NN final-state interaction (FSI) produces narrower NN prongs than would otherwise be seen.

Following Meyer *et al.* [16], we used the FSI formulation of Watson [47], Migdal [48], and Morton *et al.* [49], developed for s-wave NN scattering. The formulas used in our Monte Carlo simulation are the following:

$$w_1(T_{pn})=\left[T_{pn}+\frac{(\hbar c)^2}{m_N}\left(\frac{r_1 m_N T_{pn}}{2(\hbar c)^2}-\frac{1}{a_1}\right)^2\right]^{-1}, \quad (4)$$

$$w_3(T_{pn})=\left[T_{pn}+\frac{(\hbar c)^2}{m_N}\left(\frac{r_3 m_N T_{pn}}{2(\hbar c)^2}-\frac{1}{a_3}\right)^2\right]^{-1}, \quad (5)$$

and

$$w=\mu w_3+(1-\mu)w_1. \quad (6)$$

The w's are unnormalized weights for the effect of the FSI; they are functions of the NN center-of-mass kinetic energy, $T_{pn}=m_{pn}-m_p-m_n$. The mass m_N is the nucleon mass, taken here to be the average of the proton and neutron masses m_p and m_n; m_{pn} is the invariant mass of the proton-neutron system. The weight of the singlet NN interaction is w_1; that of the triplet is w_3. The unsubscripted w is the summed FSI interaction, with μ being the fraction of the interaction that is triplet and $(1-\mu)$ being the fraction that is singlet. The a's and r's are the scattering lengths and effective ranges, respectively; their subscripts label them as singlet or triplet. The values we used were

	singlet	triplet
scattering length	$a_1=-23.71$ fm	$a_3=+5.425$ fm
effective range	$r_1=+2.73$ fm	$r_3=+1.749$ fm

These are the empirical values for the interaction with no Coulomb force.

We determined the value of μ empirically by fitting the Monte Carlo simulation's output to our observed angular distributions. For beam energies 293 MeV$<T_{\rm beam}<$320 MeV, the results of the fit for μ were consistent with the observed singlet-to-triplet ratios found by comparing the cross sections of the (pure singlet) $pp\pi^0$ final states [16] with $pn\pi^+$ final states. Only at 330 MeV, where the approximation of pure s wave in the np interaction becomes questionable, did we observe a slight deviation from the observed value of $\mu=0.92(1)$ to match empirically the Monte Carlo results to the observed distribution. At 330 MeV, we set $\mu=1$.

Since the FSI weight w is a function of only one variable T_{pn}, the acceptance when calculated as a function of T_{pn} is insensitive to the presence, absence, or details of the FSI; the weight is present in both the accepted and initial counts, and so in the ratio of accepted to initial counts the weight cancels out. Therefore, when calculating the cross section as $d\sigma/dT_{pn}$, we need not be concerned with the effects of the FSI on the total cross section. This conclusion also holds for any variable F in $d\sigma/dF$ when F is a function of T_{pn}. When calculating the total cross sections for $pp\rightarrow pn\pi^+$, we integrate

$$\sigma_{\rm total}=\int_0^{\eta}\frac{d\sigma}{d\eta'}(\eta')d\eta', \quad (7)$$

where η', the event-by-event pion c.m. momentum fraction, is a function of T_{pn} and the beam energy. For any given beam energy, our calculation of the total cross section is independent of the details of our FSI model.

C. Luminosity monitor and cross section errors

We deduce the integrated luminosity $\mathcal{L}$ by measuring the $pp\rightarrow pp$ elastic events concurrently with the $pn\pi^+$ events using the same detectors and target. We count the elastically scattered protons that make coincidences between our drift chambers or hodoscope and one of the two position-sensitive detectors. We then compare the known elastic cross section to our measured yield to find $\mathcal{L}$.

We use as an input for our calculation those events which have good overlap in both the forward and background detectors, namely, those counts in the region where the forward laboratory angle is $8°<\theta<12°$. There the weighted average of the elastic cross sections is 17.3 mb/sr at 300 MeV, 17.8 mb/sr at 320 MeV, and 18.1 mb/sr at 330 MeV.

The details of this method have been described elsewhere [23,42,50]. Its uncertainties are dominated by three systematic errors.

(i) Geometrical acceptance. The estimated error of the active dimensions of the PSD's is ± 0.15 mm, and the estimated error of the PSD's distance from the beam is ± 2 mm. There are related discrepancies between the yields measured by the left and right PSD's. A conservative estimate of this error places it at less than 6%.

(ii) The tails of the gas-jet distribution. The contribution of the tails of the gas-jet target to the total luminosity is not observed directly. The models which deduce the tail shape have an estimated error of 3% [23].

(iii) The pp elastic cross section is known to about 4%.

The sum of the squares of these errors yields a total scale error in the integrated luminosity of about 8%.

D. Cross sections

Given an integrated luminosity $\mathcal{L}$ and a pion acceptance $a_\pi(\theta)$, we can calculate the cross section,

$$\frac{d\sigma}{d\Omega}(\theta)=\frac{1}{2\pi}\frac{d\sigma}{d\cos\theta}(\theta) \quad (8)$$

$$=\frac{1}{2\pi}\frac{1}{a_\pi(\theta)\mathcal{L}}\frac{dN_\pi}{d\cos\theta}(\theta). \quad (9)$$

Here, $\mathcal{L}$ is the integrated luminosity uncorrected for dead time, which is the effective luminosity we want, since the pion-event counts N_π share the same dead time. The notation $dN_\pi/d\cos\theta$ signifies the number of pions per unit $\cos\theta$. In this analysis, we use a bin width of $\Delta\cos\theta=1/20$, which is well inside our resolution.

The error in the scale of the $pp \rightarrow pn\pi^+$ cross sections comes from the following contributors.

(i) The total luminosity error contributes 8%.

(ii) The uncertainty in the number of good events lost in the software cuts, including the uncertainty of losses due to nuclear reactions between p and carbon in the E detectors and n and steel in the magnet pole faces, contributes 8%.

(iii) The neutron efficiency, found from the efficiency calculation described in Ref. [45], is uncertain by 5%.

(iv) The uncertainties in the positions of the detectors leading to errors in the acceptance calculations are less than 1% at energies above 300 MeV, but are 15% at 293 MeV and 4% at 297 MeV, and so they are not included in the overall scale error, but applied individually at those two energies.

The overall scale error is taken to be the sum of the squares of these contributions, or 12%.

The cross section $(d\sigma/d\Omega)(\theta)$, defined in Eq. (9), is accurate only for beams that have no polarization perpendicular to the z axis, and an appropriate average of spin-dependent cross sections must be taken. For a beam with polarization $P_\uparrow$ or $P_\downarrow$, our cross sections are

$$\sigma_{\uparrow\downarrow}(\theta,\phi)=\sigma(\theta,\phi)[1+P_{\uparrow\downarrow}A_y(\theta,\phi)]. \tag{10}$$

Here, σ is the cross section for unpolarized beam, and A_y is the analyzing power.

Eliminating A_y and solving for σ gives us

$$\sigma=\frac{(\sigma_\uparrow+\sigma_\downarrow)\overline{P}-(\sigma_\uparrow-\sigma_\downarrow)\Delta}{2\overline{P}}, \tag{11}$$

where $\overline{P}\equiv(P_\uparrow-P_\downarrow)/2$ and $\Delta\equiv(P_\uparrow+P_\downarrow)/2$. If $\Delta=0$, then this equation reduces to

$$\sigma=\frac{1}{2}(\sigma_\uparrow+\sigma_\downarrow), \tag{12}$$

which is the simple average of $\sigma_\uparrow$ and $\sigma_\downarrow$.

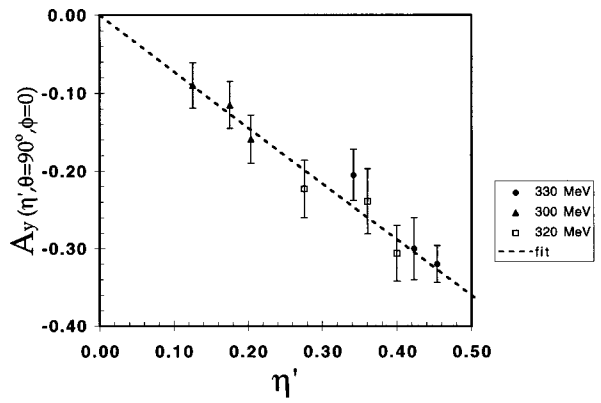

FIG. 10. Measured analyzing powers as a function of η' from the runs at $T_{\text{beam}}=300$, 320, and 330 MeV. The counts from each energy were divided up into three bins, one for low values of η', another for high, and a third for the intermediate values. A_y was determined for each bin and plotted against the mean value of η'.

E. Beam polarization

The beam polarization is measured by comparing the pp elastic cross sections to the known pp elastic analyzing power. Since the analyzing power $A_y(\theta)$ is well known [46], we can solve for the polarization,

$$P=\frac{1}{A_y(\theta)}\frac{\frac{d\sigma}{d\Omega L}(\theta)-\frac{d\sigma}{d\Omega R}(\theta)}{\frac{d\sigma}{d\Omega L}(\theta)+\frac{d\sigma}{d\Omega R}(\theta)}. \tag{13}$$

The symbols L and R designate the cross sections as measured in the left and right PSD's. The beam polarizations were measured after acceleration in the cooler, simultaneously with pion-production events.

The beam was not perfectly stable and varied from tune to tune; therefore, discrepancies between the geometric acceptances of our left and right detectors can create measurements of the polarization that are too large in one spin state and too small in the other. However, actual differences Δ in the magnitude of the up and down polarizations of greater than about 2% are very rare at IUCF, $|\Delta|<0.02$. Therefore, we have assumed in our analysis of the pion events that $\Delta=0$ and used $P_\uparrow=+\overline{P}$ and $P_\downarrow=-\overline{P}$. The calculation of the mean $\overline{P}$ does not depend on an accurate measure of Δ; the systematic geometrical acceptance errors cancel out.

As in the calculation of the luminosity, we use those scattering events which have good simultaneous acceptance in both the forward and background detectors, $8°<\theta<12°$. There the weighted average of A_y^{pp} is 0.350 at 300 MeV, 0.363 at 320 MeV, and 0.375 at 330 MeV.

IV. RESULTS

A. Analyzing powers for $pp \rightarrow pn\pi^+$

For beams with 100% polarization in the up $(+y)$ or down $(-y)$ direction, the analyzing power can be defined as

$$A_y(\theta,\phi)=\frac{\sigma_\uparrow(\theta,\phi)-\sigma_\downarrow(\theta,\phi)}{\sigma_\uparrow(\theta,\phi)+\sigma_\downarrow(\theta,\phi)}, \tag{14}$$

where $\sigma_\uparrow$ is the cross section as a function of θ and ϕ for a beam polarized up and $\sigma_\downarrow$ for a beam polarized down. Note that the angular acceptance errors cancel out of this equation.

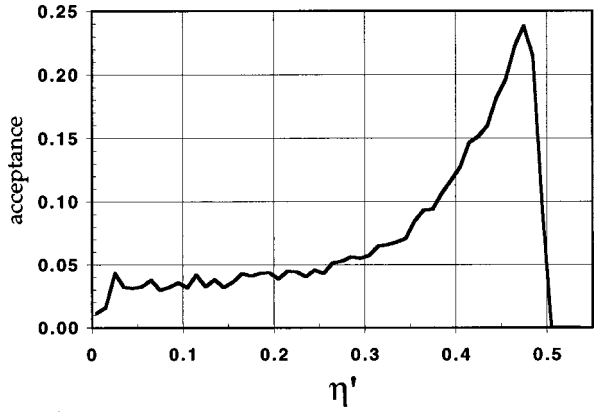

FIG. 11. Monte Carlo calculation of the c.m. pion acceptance as a function of η' at 330 MeV.

TABLE IV. The six leading terms in the partial-wave expansion for $pp \rightarrow pn\pi^+$. Notation: l, S, and J are the initial pp state orbital, spin, and total angular momentum, L is the pion angular momentum, j is the pn spin, and l_{pn} is the pn orbital angular momentum. The last column shows the notation of Rosenfeld [11] for reference.

	Initial			Final			
Ampitudes	l	S	J	L	j	l_{pn}	Channel
a_0	0	0	0	1	1	0	$^1S_0 \rightarrow {}^3S_1\ p0$
a_1	1	1	1	0	1	0	$^3P_1 \rightarrow {}^3S_1\ s1$
a_2	2	0	2	1	1	0	$^1D_2 \rightarrow {}^3S_1\ p2$
b_0	1	1	0	0	0	0	$^3P_0 \rightarrow {}^1S_0\ s0$
b_1	0	0	0	0	1	1	$^1S_0 \rightarrow {}^3P_0\ s0$
b_2	2	0	2	0	1	1	$^1D_2 \rightarrow {}^3P_2\ s2$

For real beams with average polarization $\overline{P}$, the analyzing power is calculated by

$$A_y = \frac{\epsilon}{\overline{P}}, \tag{15}$$

where ϵ is the asymmetry which we directly measure.

The counts were sorted into ϕ and cos θ bins and used to calculate $A_y(\theta,\phi)$. The result was then fit by the function of Eq. (20), described below, and the analyzing power was extracted from this fit.

Following custom, we describe our differential cross sections by fits to a Legendre polynomial expansion in cos θ,

$$\frac{d\sigma}{d\Omega}(\theta) = C_0 + C_1 P_1(\cos\theta) + C_2 P_2(\cos\theta) + \cdots, \tag{16}$$

where P_1 and P_2 are Legendre polynomials with $P_1(x)=x$ and $P_2(x)=(3x^2-1)/2$. Higher order terms were not necessary for a good fit to the cross sections. Note that $\sigma_{\text{total}} = 4\pi C_0$.

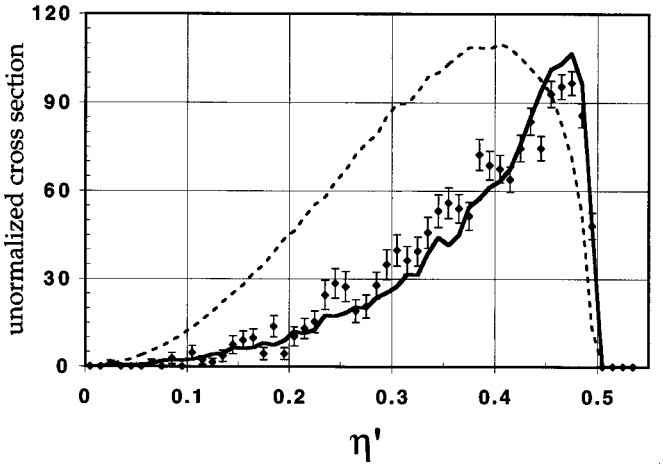

FIG. 12. Observed pion momentum distribution in the c.m., corrected for geometrical acceptance, at 330 MeV. Points with error bars show the measured cross section $d\sigma/d\eta'$ in arbitrary units. The curves show Monte Carlo simulations under two assumptions: the solid curve shows the momentum distribution with the final-state interaction, and the dashed curve shows the momentum distribution without the FSI.

Partial-wave expansion. Assuming that near-threshold states are restricted to orbital angular momenta with $1\hbar$ or less, only six partial waves have either pion L or l_{pn} equal to zero. (See Table IV.) We followed the example of Blankleider and Afnan and earlier researchers [12,51,52] who calculated the partial-wave expansion for $\vec{p}p \rightarrow d\pi^+$ with the partial-wave amplitudes of the three lowest order isoscalar channels. We added the three isovector terms for the unbound pn system [42]. Since we integrate over the relative angles and energies of the pn system, we can continue to treat the $pn\pi^+$ final state in a two-body formalism as long as we remember that the pn ''pseudodeuteron'' is not restricted in its invariant mass m_{pn} or in its angular momentum. Integration over the parameters of the pn system has the added benefit of causing the interference terms between the isoscalar and isovector partial waves, listed in Table IV, to average to zero. So Eqs. (17)–(19) which result from this expansion look similar to those found previously for $\vec{p}p \rightarrow d\pi^+$ [19].

Retaining only the first six partial waves, shown in Table IV, the observables of the $\vec{p}p \rightarrow pn\pi^+$ reaction become

$$A_y(\theta,\phi) = \sin\theta\cos\phi\ \frac{\sqrt{2}\ \mathrm{Im}[a_1 a_0^*] + \mathrm{Im}[a_1 a_2^*]}{4\frac{d\sigma}{d\Omega}(\theta)}, \tag{17}$$

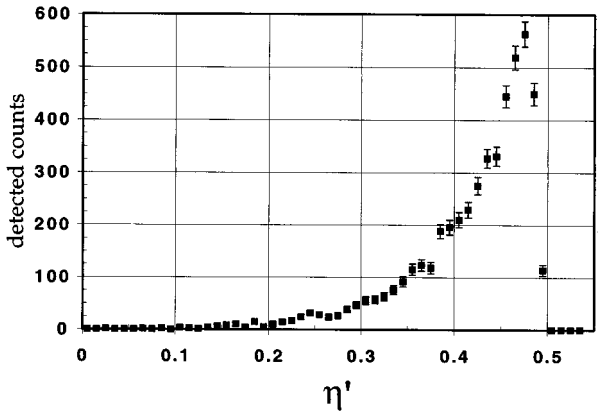

FIG. 13. Observed pion counts as a function of η' before correction for acceptance, 330 MeV.

TABLE V. Analyzing power A_{N0} derived from fits to the $A_y(\theta,\phi)$ measurements, which are corrected for the η' acceptance. The right column shows the chi squared per degree of freedom of the fit.

Energy	η	A_{N0}	χ^2
300 MeV	0.22	-0.127 ± 0.022	1.22
320 MeV	0.42	-0.244 ± 0.027	0.87
330 MeV	0.50	-0.275 ± 0.032	0.94

TABLE VI. List of differential cross section parameters at 300, 320, and 330 MeV. Errors shown do not include a 12% systematic scale error which equally affects both C_0 and C_2, but which does not affect the ratio $B=C_2/C_0$.

η	C_0 (μb)	C_2 (μb)	$B=C_2/C_0$
0.22	0.380 ± 0.015	0.057 ± 0.038	0.15 ± 0.10
0.42	3.24 ± 0.13	1.04 ± 0.22	0.32 ± 0.07
0.50	5.39 ± 0.21	1.99 ± 0.43	0.37 ± 0.08

$$C_0=\frac{|a_0|^2}{4}+\frac{|a_1|^2}{4}+\frac{|a_2|^2}{4}+\frac{|b_0|^2}{12}+\frac{|b_1|^2}{4}+\frac{|b_2|^2}{4}, \tag{18}$$

$$C_2=\frac{1}{4}|a_2|^2-\frac{1}{\sqrt{2}}\,\mathrm{Re}[a_0a_2^*], \tag{19}$$

and $C_1=0$.

Because these equations are so simple, it is possible to describe them in terms of the two observables $A_{N0}\equiv A_y(\theta=90°,\phi=0°)$ and $B\equiv C_2/C_0$. The ratio B is determined from cross-section fits to Eq. (16). To determine A_{N0}, the experimental results from Eq. (14) are fit to

$$A_y(\theta,\phi)=A_{N0}\left(1-\frac{1}{2}B\right)\frac{\sin\theta}{1+BP_2(\cos\theta)}\cos(\phi). \tag{20}$$

The scale errors in the cross section cancel out of the calculation of both A_{N0} and B.

The counts in the measured angular distributions near $\cos\theta=-1$ and $\cos\theta=+1$ are sensitive to the exact placement of our missing mass cut. To avoid errors introduced by this sensitivity, we fit the analyzing power to counts in the region away from these points, where the analyzing power is largest, $-0.75<\cos\theta<+0.75$.

The dependence of A_y on the pion momentum is shown in Fig. 10. There the asymmetry is calculated as a function of η', the pion momentum fraction for any particular event (as distinct from η, the maximum possible pion momentum fraction for a given incident energy). A linear function fits these data well and suggests that the analyzing power in this energy region is proportional to η'. Since our detector acceptance is not generally uniform in η', this means we must correct for our acceptance. Figure 11 shows our least uniform η' acceptance which is at 330 MeV. Since the acceptance is enhanced at large η' and therefore large analyzing power, the correct mean analyzing power is somewhat smaller than the observed mean. The correction factor at 330 MeV is the ratio of the mean value of the η' distribution in Fig. 12 to the mean in Fig. 13. The correction factors at the other energies were deduced from similar plots, not shown. At 300 MeV, the correction factor is 0.99(1); at 320 and 330 MeV, the corrections are 0.92(1).

The results including these corrections are shown in Table V. Here, A_{N0} was found by making fits to the data binned into a grid of 96 bins, 8 in $\cos\theta$ and 12 in ϕ, using Eq. (20). The fits used the values of B shown in Table VI. (The determination of B is described in Sec. IV B, below.) Changes in B of ±0.30 did not alter the fits for A_{N0} outside of the quoted error bars, and so the A_{N0}'s are almost entirely independent of acceptance errors in the determination of B. Errors for A_{N0} at all energies are dominated by statistics.

Figures 14 and 15 show projections of the angular distributions with error bars, and the fit for the corresponding A_{N0} and B as a projection of Eq. (20).

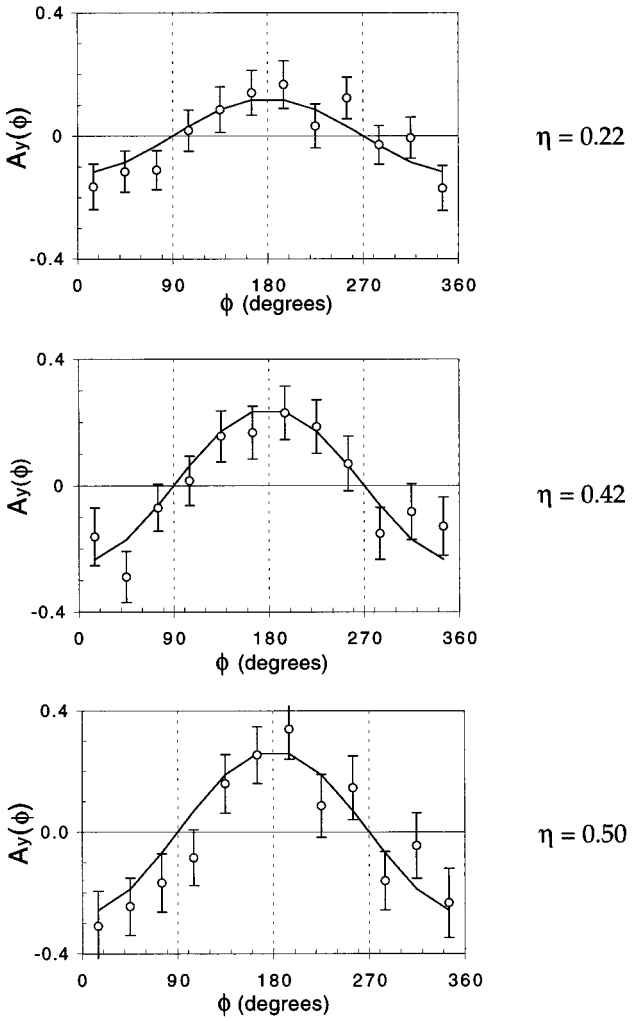

FIG. 14. $A_y(\phi)$ at $T_{\mathrm{beam}}=300$, 320, and 330 MeV. Plotted points show A_y integrated over $-0.5<\cos\theta<+0.5$ and corrected for η' acceptance and angular resolution. The curve shows the results of a fit of the partial-wave equations to the two-dimensional $A_y(\theta,\phi)$ data, as discussed in the text.

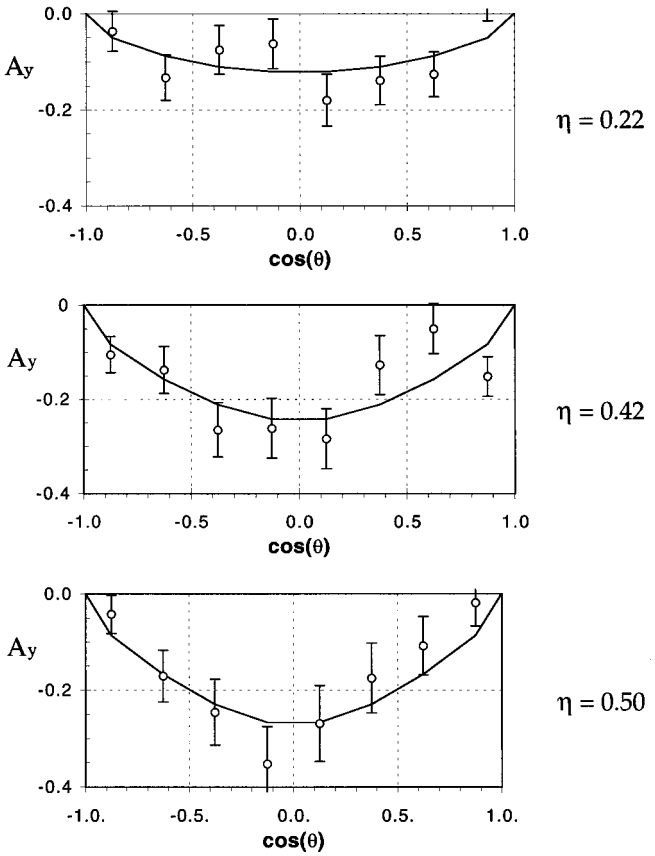

FIG. 15. $A_y(\theta)$ at $T_{\text{beam}}=300$, 320, and 330 MeV. Plotted points show A_y integrated over $-0.86<\cos\phi<+0.86$, corrected for η' acceptance and angular resolution. The curve shows the results of a fit of the partial-wave equations to the two-dimensional $A_y(\theta,\phi)$ data.

B. Cross sections

The differential cross sections are well fit by the first three terms of formula (16). Early in the analysis, systematic errors in our energy calibration caused the differential cross sections calculation to show asymmetries about $\cos\theta=0$. After using our most careful energy calibrations, we are left with only slight asymmetries in $\cos\theta$. We do not believe that these remaining asymmetries are physical. Fits to the differential cross section yield values of C_1 within one standard deviation ($\sigma=0.02$) of zero, and the calculation of the first six partial waves produces no C_1 term; so we have set $C_1=0$ in our final analysis.

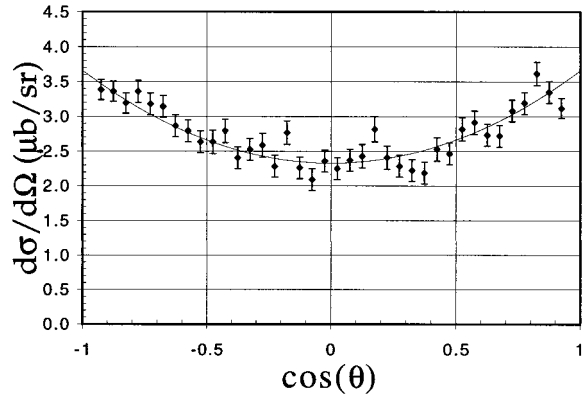

FIG. 17. 320 MeV: differential cross section with fit to the Legendre expansion described in the text.

Only three of our seven beam energies yielded enough statistics to allow us to reliably extract the parameters C_0 and C_2. These are the 300-, 320-, and 330-MeV runs. Table VI shows a summary of the fits. Plots of the cross sections are shown in Figs. 16–18, along with the fits which resulted. The fit to the 300-MeV data has a $\chi^2_{\text{p.d.f.}}$ (chi squared per degree of freedom) of 1.02, the 320-MeV fit has a $\chi^2_{\text{p.d.f.}}$ of 1.22, and the 330-MeV fit has a $\chi^2_{\text{p.d.f.}}$ of 1.00.

The errors shown for C_0 are random and do not reflect the scale errors noted in the previous section. The errors in the extraction of C_2 are due almost entirely to the sensitivity of this parameter to our Monte Carlo acceptance.

Total cross sections. Figure 19 and Table VII show the total cross section for all seven beam energies as a function of pion η. We show only the random errors for the five highest energies. At $\eta=0.07$ and $\eta=0.17$, systematic errors in θ_{lab} due to the uncertainty of the beam direction are also included; at higher energies, this error is insignificant. At the $\eta=0.07$ point, there is also an uncertainty in the η value due to the fact that our beam energy is not known to better than 100 keV. This uncertainty is too small to plot at 300 MeV and higher energies. All points have a common 12% scale error in the cross section due to uncertainties in the luminosity monitor and pion cuts.

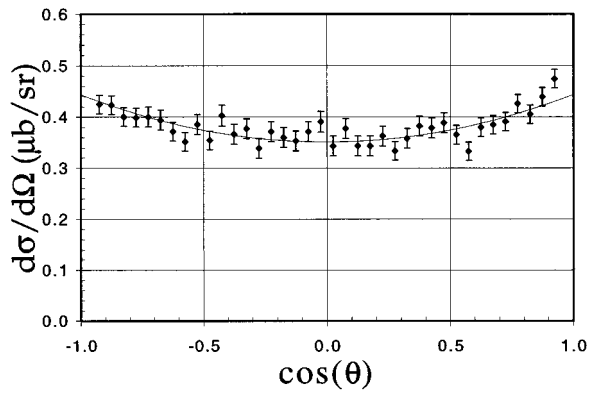

FIG. 16. 300 MeV: differential cross section with fit to the Legendre expansion described in the text.

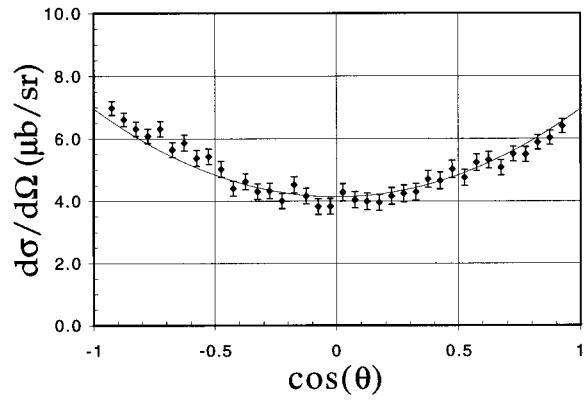

FIG. 18. 330 MeV: differential cross section with fit to the Legendre expansion described in the text.

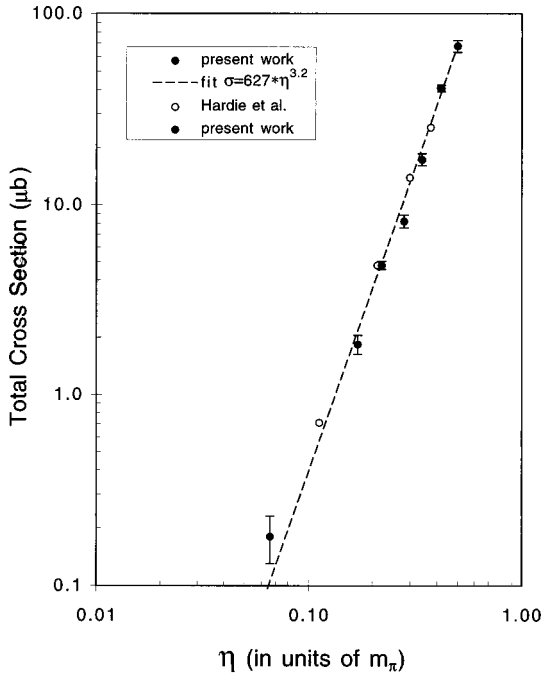

FIG. 19. Total cross sections for $pp \rightarrow pn\pi^+$. Random errors for the present work are shown where they exceed the symbol size. The scale has a 12% systematic error.

The total cross sections were found by integrating over the pion momentum distribution which is independent of the final-state interaction. It can also be found by integrating over the pion angular distribution, which is sensitive to the FSI. Comparing the two methods provides a cross-check against mistakes in the calculation and also yields an estimate for errors in the final-state interaction. The largest discrepancy (3%) outside of statistical uncertainties is found at 330 MeV where the FSI may no longer be a simple function of η'. It was at 330 MeV where the empirical value of $\mu = 1$, mentioned above, was incompatible with the observed singlet-triplet mixing of $\mu = 0.92(1)$.

Two anomalous cross sections. The data for beam energies 297 and 305 MeV are from the last two runs in 1995. They followed the other runs after 1.5 days of retuning the accelerator and fixing equipment failures. When beam was returned to the target, the beam-target intersection was noticeably different from what it had been for the previous five

TABLE VII. Total cross sections for $pp \rightarrow pn\pi^+$. The listed errors do not include an overall 12% scale error which applies to all points. The 297 and 305 cross sections may have an undiscovered systematic error of ~25% related to equipment problems that occurred during data taking (see text).

Energy	η	Cross section (μb)
293 MeV	0.07	0.16±0.04
297 MeV	0.17	1.84±0.18
300 MeV	0.22	4.8±0.2
305 MeV	0.28	8.2±0.4
310 MeV	0.34	17.3±0.7
320 MeV	0.42	40.8±1.6
330 MeV	0.50	67.8±2.7

TABLE VIII. The partial-wave phase shifts for $pp \rightarrow pp$ elastic scattering for the states corresponding to the isosinglet final states of $pp \rightarrow pn\pi^+$, shown for three different beam energies, expressed as pion η.

η (m_π)	0.22	0.42	0.50
δ_0	−6.13°	−8.32°	−9.37°
δ_1	−28.7°	−30.0°	−30.6°
δ_2	9.09°	9.49°	9.69°
$\sin(\delta_1-\delta_0)$	−0.38	−0.37	−0.36
$\sin(\delta_1-\delta_2)$	−0.61	−0.64	−0.65
$\cos(\delta_2-\delta_0)$	0.965	0.952	0.945

energies. This difference made necessary a new correction to the luminosity calculation for the tails of the gas-jet target, which has been made and implemented in the present analysis. However, the cross sections for these two runs are still ~25% lower than one might expect from simple extrapolations from the other cross sections. It is conceivable that a large systematic error in these two runs went unnoticed by us and remains uncorrected in the cross-section calculation.

V. PARTIAL-WAVE SOLUTIONS

We calculate the partial-wave amplitudes for three beam energies from the $P_2(\cos\theta)$ strength and the analyzing power. To find a_0, a_1, and a_2, we make use of the three phases δ_0, δ_1, and δ_2, predicted using Watson's theorem (see Refs. [53,10,12,19]), taking the $pp \rightarrow pn\pi^+$ phase shifts from the dominant $pp \rightarrow pp$ elastic reaction. We also use the observables C_0, C_2, and A_{N0}, which we found from the cross sections. These energy-dependent values are shown in Table VIII, and are related to the partial-wave amplitudes by the equations

$$a_0 = \pm|a_0|e^{i\delta_0}, \tag{21}$$

$$a_1 = \pm|a_1|e^{i\delta_1}, \tag{22}$$

$$a_2 = \pm|a_2|e^{i\delta_2}. \tag{23}$$

The isovector strengths cannot be extracted from the measurements of this experiment, but their sum is known from the cross sections measured by Meyer *et al.* [16] for the reaction $pp \rightarrow pp\pi^0$. Since the pp final state cannot contain isoscalar partial waves, Eq. (18) becomes simply

$$C_0^{pp\pi^0} = \frac{1}{12}|b_0|^2 + \frac{1}{4}|b_1|^2 + \frac{1}{4}|b_2|^2. \tag{24}$$

To interpolate between the $pp\pi^0$ points and our own values of η, we used the formula $\sigma_{pp\pi^0} = (28.95\ \mu\text{b})\,\eta^{(2.3)}$, which resulted from a fit over the range $0.22 < \eta < 0.50$. Judging by the goodness of the fit to the cross sections of Ref. [16], shown in Fig. 20, the error in $C_0^{pp\pi^0}$ is about 4%. The relative error between the isoscalar a contributions and the isovector b contributions is dominated by the scale error in the $pn\pi^+$ cross sections, for a total error of 13%.

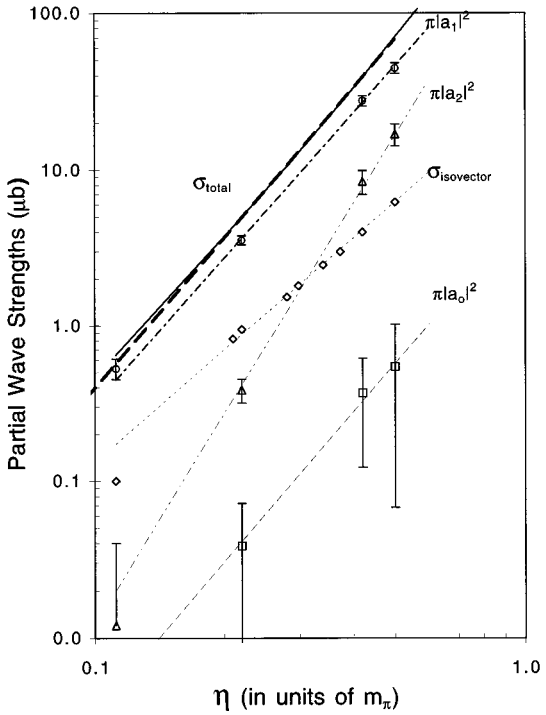

FIG. 20. Cross sections of the first six partial waves as a function of η. Error bars do not include the overall 12% scale error. The squares represent the values of $\pi|a_0|^2$, the circles are $\pi|a_1|^2$, and the triangles are $\pi|a_2|^2$. The diamonds indicate the total cross-section measurements of [16] for isovector $pp\pi^0$ final states, $\sigma_{\text{isovector}}=\pi(|b_0|^2/3+|b_1|^2+|b_2|^2)$. Each set of amplitudes is fit to a simple $\sigma\propto\eta^n$ function; the sum of all the functions is the solid curve. It is barely distinguishable from a fit to the total cross sections (taken from the present work and from [23]), shown as a heavy dashed line. The $\eta=0.11$ isoscalar points are taken from [23].

A. Solving for the partial-wave amplitudes

We use Eqs. (16)–(19) to solve for $|a_1|$ in terms of $|a_0|$ and $|a_2|$, and to solve for $|a_2|$ in terms of $|a_0|$, to get

$$|a_1|=\frac{2A_{N0}(2-B)C_0}{\pm\sqrt{2}|a_0|\sin(\delta_1-\delta_0)\pm|a_2|\sin(\delta_1-\delta_2)} \tag{25}$$

and

$$|a_2|=\pm\sqrt{2}|a_0|\cos(\delta_0-\delta_2)\pm 2\sqrt{B\pm\frac{1}{2}|a_0|^2\cos^2(\delta_0-\delta_2)}. \tag{26}$$

To solve for $|a_0|$ we plot $|a_1|$ and $|a_2|$ as a function of $-|a_0|$ and $+|a_0|$ and then find the intercept of $|a_1|$ and $|a_2|$.

The solutions for the partial-wave amplitudes. The three equations (18), (25), and (26) yield several sets of solutions for the three unknowns $|a_0|$, $|a_1|$, and $|a_2|$ because of the various choices of sign allowed by the equations. Choosing the right sign is usually obvious; it is desirable, for instance, that the magnitudes of partial-wave amplitudes be positive and noncomplex, and thus negative or complex solutions are rejected. The choice of sign can be arbitrary; a different choice can yield equivalent solutions. After the obvious choices are made, we are still left with two choices for the solutions at 320 and 330 MeV, and four choices at 300 MeV.

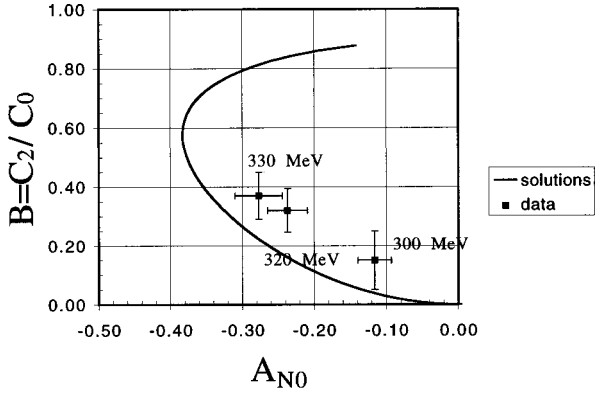

FIG. 21. Relationship of B and A_{N0}. The curve assumes $a_0/e^{i\delta_0}=0$. The observed data at 320 or 330 MeV are not compatible with the assumption that $a_0=0$.

B. Physical considerations in the partial-wave solutions

As we climb in energy, we expect the $\Delta(1232)$ resonance to become increasingly important. This increasing strength will express itself as a larger a_2 contribution to the cross section. At the same time, we see a smoothly increasing B and A_{N0}, as shown by our data and in the $pp\rightarrow d\pi^+$ reaction [19].

The solution consistent with gradually increasing $|a_2|$, B, and A_{N0} is the most realistic one. Given a value of $|a_0|$ (from, for instance, one of our solutions), it is possible to calculate A_{N0} and B as functions of $|a_2|$.

An example is plotted in Fig. 21 which shows the relationship between the angular distribution observable B and the analyzing power A_{N0} assuming that $|a_0|=0$. This assumption was made previously, by necessity, before analyzing powers were available [23]. Now that values for A_{N0} have been measured, we can see that the $|a_0|=0$ curve misses the data.

Making different assumptions about the value of $|a_0|$, Fig. 22 shows the relationship between the observables A_{N0}

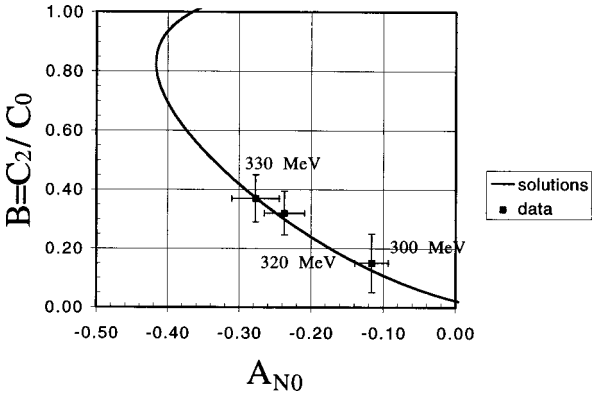

FIG. 22. Relationship of B and A_{N0}. The curve uses $a_0/e^{i\delta_0}=-0.18\sqrt{C_0}$ and represents the chosen solution for 330 MeV. Other plots (not shown), with similar values of a_0, produce curves which intersect the 320 and 300 MeV data points.

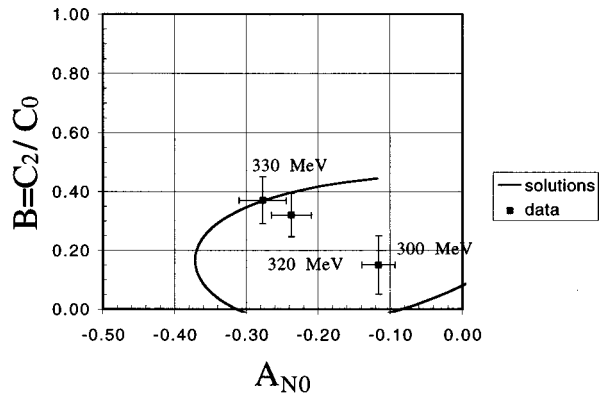

FIG. 23. Relationship of B and A_{N0}. The curve uses $a_0/e^{i\delta_0}=+0.34\sqrt{C_0}$ and yields a solution for 330 MeV. While $a_0/e^{i\delta_0}=+0.34\sqrt{C_0}$ is a mathematically valid solution, it is disregarded for physical reasons.

and B. The solid curve shows the calculated set of solutions which vary with $|a_2|$, which parametrizes the curve. At the bottom right corner of the plot, $|a_2|$ is near zero. As it increases, the value of B also increases. The points with error bars show the location of our data, plotting the observed A_{N0} versus the observed B. All three beam energies are shown, from 300 MeV (lower right) to 330 MeV (upper left). The intersection of the curve with the data indicates a solution of $|a_0|$ and the parameter $|a_2|$. Figure 23 shows a solution for 330 MeV that does not exhibit the expected correlation between B and A_{N0}, and so we reject it in favor of the more realistic solution of Fig. 22. Individual solutions were also found for the 300- and 320-MeV runs (not shown here).

C. Summary of solutions with errors

We have physically realistic solutions for the partial-wave amplitudes at all three energies as shown in Table IX. The $|a_0|$ errors were found by seeing how much we can vary our solution for $|a_0|$ and still make curves that fall within our B error bars. The $|a_2|$ errors were obtained by finding over what range we can vary $|a_2|$ and still get values of A_{N0} that fall within the plotted error bars. Errors in $|a_1|$ were calculated from the errors in a_0, a_2, and the isovector strength by applying standard error propagation techniques to Eq. (18). The phases from Watson's theorem have errors of $\sim 1°$, but the uncertainties they cause are an order of magnitude smaller than those caused by errors in B and A_{N0}.

Table X gives a summary of the partial waves as fractions of the total cross sections, assuming that only the first six partial waves contribute. Figure 20 shows the individual absolute partial-wave cross sections in μb.

TABLE IX. Values for $pp\rightarrow pn\pi^+$ partial-wave amplitudes, with errors, at three different beam energies. The amplitudes are in units of $\sqrt{C_0}$.

η	a_0/e^{δ_0}	a_1/e^{δ_1}	a_2/e^{δ_2}
0.22	-0.18 ± 0.14	$+1.72\pm0.06$	$+0.57\pm0.05$
0.42	-0.19 ± 0.07	$+1.65\pm0.06$	$+0.91\pm0.08$
0.50	-0.18 ± 0.08	$+1.63\pm0.06$	$+1.00\pm0.08$

TABLE X. Partial-wave fractional cross sections for $pp\rightarrow pn\pi^+$. Partial-wave strengths expressed as a fraction of the total cross section, assuming only six waves contribute. The $L=0$ waves are a_1 and the b waves.

η	a_0 strength	a_1 strength	a_2 strength	b strength
0.22	0.008 ± 0.013	0.74 ± 0.05	0.080 ± 0.014	0.173 ± 0.022
0.42	0.009 ± 0.006	0.68 ± 0.05	0.207 ± 0.036	0.105 ± 0.013
0.50	0.008 ± 0.007	0.66 ± 0.05	0.250 ± 0.040	0.085 ± 0.011

VI. SUMMARY AND CONCLUSIONS

The new total cross sections for $pp\rightarrow pn\pi^+$ extend the near-threshold data from $\eta=0.11$ down to $\eta=0.07$ and from $\eta=0.42$ up to $\eta=0.50$. In the range of overlap, the new measurements agree within errors with the earlier results [23]. New differential cross sections at $\eta=0.50$ serve to quantify the onset of the P wave at energy regions above threshold.

The observed analyzing powers grow almost linearly with η', independently of the incident beam energy. The analyzing powers for the $pn\pi^+$ final state are the same sign, but approximately half the magnitude, of those for the $\vec{p}p\rightarrow d\pi^+$ reaction. This is partly due to the unbound pn state taking more of the final-state energy than the bound deuteron can. In addition, the presence of the isotropic isovector partial waves, absent for the bound np case, dilutes the asymmetry in the cross section. The work of Fäldt and Wilkin [36] accounts for much of this difference.

The new analyzing power measurements for the first time enable a clean partial-wave analysis of this reaction under the assumption that only the six lowest order partial waves contribute. This analysis shows that the isoscalar s wave dominates the reaction even at energies as high as 330 MeV, where it makes up 66% of the cross section. For the range $0.1<\eta<0.5$ the partial-wave contributions increase monotonically with powers of η. The most dominant contribution, the $L_\pi=0$ isoscalar channel, can be represented by $|a_1|^2 \propto \eta^{3.2}$. The smaller $L_\pi=1$ channels rise significantly faster and will become dominant at $\eta=1$ if the monotonic increase continues.

This model-independent determination of the partial-wave amplitudes provides a quantitative measure of the s-wave strength for emitted pions relative to the pair of final-state nucleons. The ultimate interpretation of this information would be in terms of the πNN off-shell form factor as discussed in the Introduction. Before this can be done, the transformation to the πN frame must be made and the so-called ''heavy meson'' contribution [26] must be subtracted. First indications are that while the heavy-meson contribution can be a major component of the $L_\pi=0$ amplitude for $pp\rightarrow pp\pi^0$, it is a much smaller component for $pp\rightarrow pn\pi^+$ [6,38].

The quantitative measurement of the $L_\pi=0$, $l_{pn}=0$ channel also makes possible a comparison with simple calculations that assume contributions from the s wave only [6,13,25–28]. More ambitious calculations have been fin-

ished recently by Hanhart [39] which seek to explain these newly observed analyzing powers and cross sections. There is growing evidence that the new data will permit the controlled study of the πNN vertex in this reaction.

Note added in proof. Since the completion of this analysis, a new experiment which measures the π^+ directly has been performed [54]. In the energy region where the two experiments overlap (320–330 MeV) the preliminary reports of the analyzing power are in good agreement with the results reported here.

ACKNOWLEDGMENTS

Special thanks are due to Keith Solberg and Alan Eads of IUCF for their assistance in building DC3 and for advice in maintaining the drift chambers. This experiment was funded by the National Science Foundation.

[1] T. Ericson and W. Weise, *Pions and Nuclei* (Oxford Science Publications, New York, 1988), Chap. 3.
[2] E. Hernández and E. Oset, Phys. Lett. B **350**, 158 (1995).
[3] C. A. Domínguez, Phys. Rev. D **27**, 1572 (1983).
[4] J. Vogelzang, B. L. G. Bakker, and H. J. Boersma, Nucl. Phys. **A452**, 644 (1986).
[5] B. C. Pearce and B. K. Jennings, Nucl. Phys. **A528**, 655 (1991).
[6] T.-S. H. Lee, in Los Alamos Report No. nucl-th/9502005 (unpublished).
[7] R. Machleidt, K. Holinde, and C. Elster, Phys. Rep. **149**, 1 (1987).
[8] V. G. J. Stoks, R. A. M. Klop, C. P. F. Terhagen, and J. J. deSwart, Phys. Rev. C **49**, 2950 (1994).
[9] G. Holzwarth and R. Machleidt, Phys. Rev. C **55**, 1088 (1997).
[10] M. Gell-Mann and K. M. Watson, Annu. Rev. Nucl. Sci. **4**, 219 (1954).
[11] A. H. Rosenfeld, Phys. Rev. **96**, 139 (1954).
[12] A. E. Woodruff, Phys. Rev. **117**, 1113 (1960).
[13] D. S. Koltun and A. Reitan, Phys. Rev. **141**, 1413 (1966).
[14] M. E. Schillaci, R. R. Silbar, and J. E. Young, Phys. Rev. **179**, 1539 (1969).
[15] H. O. Meyer, M. A. Ross, R. E. Pollock, A. Berdoz, F. D. J. E. Goodwin, M. G. Minty, H. Nann, P. V. Pancella, S. F. Pate, B. V. Przewoski, T. Rinckel, and F. Sperisen, Phys. Rev. Lett. **65**, 2846 (1990).
[16] H. O. Meyer, H. Nann, P. V. Pancella, S. F. Pate, R. E. Pollock, B. V. Przewoski, T. Rinckel, M. A. Ross, and F. Sperisen, Nucl. Phys. **A539**, 633 (1992).
[17] A. Bondar *et al.*, Phys. Lett. B **356**, 8 (1995).
[18] M. Drochner *et al.*, Phys. Rev. Lett. **77**, 454 (1996).
[19] E. Korkmaz, J. Li, D. A. Hutcheon, R. Abegg, J. B. Elliot, L. G. Greeniaus, D. J. Mack, C. A. Miller, and N. L. Rodning, Nucl. Phys. **A535**, 637 (1991).
[20] P. Heimberg *et al.*, Phys. Rev. Lett. **77**, 1012 (1996).
[21] W. R. Falk, E. G. Auld, G. Giles, G. Jones, G. L. Lolos, W. Ziegler, and P. L. Walden, Phys. Rev. C **32**, 1972 (1985).
[22] W. W. Daehnick, S. A. Dytman, J. G. Hardie, W. K. Brooks, R. W. Flammang, L. Bland, W. W. Jacobs, P. V. Pancella, T. Rinckel, J. D. Brown, and E. Jacobsen, Phys. Rev. Lett. **74**, 2913 (1995).
[23] J. G. Hardie, S. A. Dytman, W. W. Daehnick, W. K. Brooks, R. W. Flammang, L. C. Bland, W. W. Jacobs, P. V. Pancella, T. Rinckel, J. D. Brown, and E. Jacobsen, Phys. Rev. C **56**, 20 (1997).
[24] W. W. Daehnick, R. W. Flammang, S. A. Dytman, D. J. Tedeschi, R. A. Thompson, T. Vrana, C. C. Foster, J. G. Hardie, W. W. Jacobs, T. Rinckel, E. J. Stephenson, P. V. Pancella, and W. K. Brooks, Phys. Lett. B **423**, 213 (1998).
[25] G. A. Miller and P. U. Sauer, Phys. Rev. C **44**, R1725 (1991).
[26] T.-S. H. Lee and D. O. Riska, Phys. Rev. Lett. **70**, 2237 (1993).
[27] C. Horowitz, H. O. Meyer, and D. Griegel, Phys. Rev. C **49**, 1337 (1993).
[28] J. A. Niskanen, Phys. Lett. B **289**, 227 (1992).
[29] B.-Y. Park, F. Myhrer, J. R. Morones, T. Meisner, and K. Kubodera, Phys. Rev. C **53**, 1519 (1996).
[30] T. Cohen, J. Friar, G. Miller, and U. van Kolck, Phys. Rev. C **53**, 2661 (1996).
[31] J. A. Niskanen, Phys. Rev. C **53**, 526 (1996).
[32] C. Hanhart, J. Haidenbauer, A. Reuber, C. Schütz, and J. Speth, Phys. Lett. B **358**, 21 (1995).
[33] J. Haidenbauer, C. Hanhart, and J. Speth, Acta Phys. Pol. B **27**, 2893 (1996).
[34] T. Sato, T.-S. H. Lee, F. Myhrer, and K. Kubodera, Phys. Rev. C **56**, 1246 (1997).
[35] G. Fäldt and C. Wilkin, Phys. Lett. B **382**, 209 (1996).
[36] G. Fäldt and C. Wilkin, Phys. Rev. C **56**, 2067 (1997).
[37] A. Engel, R. Shyam, U. Mosel, and A. K. Dutt-Mazumder, Nucl. Phys. **A603**, 387 (1996).
[38] R. Shyam and U. Mosel, Phys. Lett. B (in press). See also nucl-th/9611013.
[39] C. Hanhart, Ph.D. thesis, University of Bonn, 1997.
[40] G. East (private communication).
[41] D. A. Hutcheon, W. C. Olsen, H. S. Sherif, R. Dymarz, J. M. Cameron, J. Johansson, P. Kitching, P. R. Liljestrand, W. J. McDonald, C. A. Miller, G. C. Neilson, D. M. Sheppard, D. K. McDaniels, J. R. Tinsley, P. Schwandt, L. W. Swenson, and C. E. Stronach, Nucl. Phys. **A483**, 429 (1988).
[42] R. W. Flammang, Ph.D. thesis, University of Pittsburgh, 1997.
[43] E. Houston, Master's thesis, University of Pittsburgh, 1993.
[44] W. W. Daehnick, W. K. Brooks, S. K. Saha, and D. O. Kreithen, Nucl. Instrum. Methods Phys. Res. A **320**, 290 (1992).
[45] R. A. Cecil, B. D. Anderson, and R. Madey, Nucl. Instrum. Methods **161**, 439 (1979).
[46] R. Arndt, C. H. Oh, I. Strakovsky, R. Workman, and F. Dohrman, Phys. Rev. C **56**, 3005 (1997).
[47] K. M. Watson, Phys. Rev. **88**, 1163 (1952).
[48] A. B. Migdal, Sov. Phys. JETP **1**, 2 (1955).
[49] B. J. Morton, E. E. Gross, E. V. Hungerford, J. J. Malanify, and A. Zucker, Phys. Rev. **169**, 825 (1968).
[50] J. G. Hardie, Ph.D. thesis, University of Pittsburgh, 1993.
[51] F. Mandl and T. Regge, Phys. Rev. **99**, 1478 (1955).
[52] B. Blankleider and I. R. Afnan, Phys. Rev. C **31**, 1380 (1985).
[53] M. L. Goldberger and K. M. Watson, *Collision Theory*, 3rd ed. (John Wiley and Sons, New York, 1964), Chap. 9, p. 533.
[54] Swapan K. Saha *et al.*, Bull. Am. Phys. Soc. **43**, 1077 (1998).